JACS
JOURNAL OF THE AMERICAN CHEMICAL SOCIETY
Article
pubs.acs.org/JACS

Electrochemical Catalyst–Support Effects and Their Stabilizing Role for IrO_x Nanoparticle Catalysts during the Oxygen Evolution Reaction

Hyung-Suk Oh,[†] Hong Nhan Nong,[†] Tobias Reier,[†] Arno Bergmann,[†] Manuel Gliech,[†] Jorge Ferreira de Araújo,[†] Elena Willinger,[‡] Robert Schlögl,[‡] Detre Teschner,*[,‡] and Peter Strasser*[,†]

[†]The Electrochemical Energy, Catalysis, and Materials Science Laboratory, Department of Chemistry, Chemical Engineering Division, Technical University Berlin, Berlin 10623, Germany

[‡]Fritz-Haber-Institut der Max-Planck-Gesellschaft, Abteilung Anorganische Chemie, Berlin 14195, Germany

Supporting Information

ABSTRACT: Redox-active support materials can help reduce the noble-metal loading of a solid chemical catalyst while offering electronic catalyst–support interactions beneficial for catalyst durability. This is well known in heterogeneous gas-phase catalysis but much less discussed for electrocatalysis at electrified liquid–solid interfaces. Here, we demonstrate experimental evidence for electronic catalyst–support interactions in electrochemical environments and study their role and contribution to the corrosion stability of catalyst/support couples. Electrochemically oxidized Ir oxide nanoparticles, supported on high surface area carbons and oxides, were selected as model catalyst/support systems for the electrocatalytic oxygen evolution reaction (OER). First, the electronic, chemical, and structural state of the catalyst/support couple was compared using XANES, EXAFS, TEM, and depth-resolved XPS. While carbon-supported oxidized Ir particle showed exclusively the redox state (+4), the $Ir/IrO_x/ATO$ system exhibited evidence of metal/metal–oxide support interactions (MMOSI) that stabilized the metal particles on antimony-doped tin oxide (ATO) in sustained lower Ir oxidation states ($Ir^{3.2+}$). At the same time, the growth of higher valent Ir oxide layers that compromise catalyst stability was suppressed. Then the electrochemical stability and the charge-transfer kinetics of the electrocatalysts were evaluated under constant current and constant potential conditions, where the analysis of the metal dissolution confirmed that the ATO support mitigates Ir^{z+} dissolution thanks to a stronger MMOSI effect. Our findings raise the possibility that MMOSI effects in electrochemistry—largely neglected in the past—may be more important for a detailed understanding of the durability of oxide-supported nanoparticle OER catalysts than previously thought.

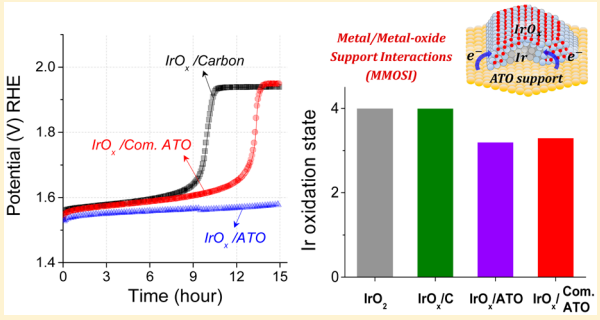

1. INTRODUCTION

Polymer electrolyte membrane (PEM) water electrolysis is an attractive and efficient method to produce pure hydrogen in connection with a renewable energy system.[1−3] However, commercialization of PEM water electrolyzers (PEMWE) has been obstructed by the use of highly expensive metal–oxide catalysts for oxygen evolution reaction (OER), such as RuO_2, IrO_2, and $Ru_{1-x}Ir_xO_2$.[4−7] Therefore, minimizing the kinetic overpotential combined with lowering the catalyst loading and thus reducing cost at improved system efficiency has been an important goal in water splitting catalysis.[8,9] One way of achieving this is to add the non-noble element (Ta, Ti, Sb, Nb, Sn) as dispersing or stabilizing agents in the dimensionally stable anodes (DSAs) system.[10−12] However, DSAs are unsuitable for use in PEMWE due to the difficulty in obtaining good contact between the electrocatalyst layer and the electrolyte membrane so that powder-type catalyst is generally applied as an ink onto the membrane.[13] An alternative way to reduce the catalyst loading in PEMWE is to utilize catalyst supports, which help to increase the dispersion and to reduce the agglomeration of the active electrocatalysts.[14−16] Typically, carbon is the most popular and probably most widely used support material in electrochemistry, because of its large surface area, high electrical conductivity, tunable graphitization, and pore structure.[15,17,18] During long-term operation of PEMWE, however, carbon can be easily oxidized to CO_2, resulting in the release of attached catalyst nanoparticles.[19−21] Furthermore, the weak interaction between the carbon support and the electrocatalyst leads to sintering of the metal–oxide nanoparticles and eventually a rapid degradation of PEMWE performance.[22−24]

To address these issues, several studies have focused on developing alternative support materials to carbon.[25−27] Among various candidates, metal–oxides are the most prevalent support material, because they have a good corrosion resistance and exhibit strong interaction with the catalyst nanoparticles.[28−30] Xia et al. studied $Nb_{0.05}Ti_{0.95}O_2$ as potential noncarbon support for IrO_2 catalyst in PEMWE.[31] The IrO_2 loading of 26 wt % provided the best mass-based activity at 1.6

Received: July 12, 2016
Published: August 23, 2016

DOI: 10.1021/jacs.6b07199
J. Am. Chem. Soc. 2016, 138, 12552−12563

V_{RHE} (471 A $g_{IrO_2}^{-1}$), which was 2.4-fold larger than that of unsupported IrO_2 (198 A $g_{IrO_2}^{-1}$). The stability of IrO_2/$Nb_{0.05}Ti_{0.95}O_2$ was also significantly improved as compared to the unsupported IrO_2 due to the anchoring effect onto the support. Additionally, previous work in our group has demonstrated that specifically prepared antimony-doped tin oxide (ATO) with a high surface area exhibited a very favorable electrochemical stability in acidic environments.[32] Ir nanodendrites (Ir-ND) and $IrNi_x$@IrO_x were supported on synthesized mesoporous ATO for water splitting.[33] Ir-ND/ATO catalyst displayed a more than 2-fold larger kinetic water splitting activity compared with IrO_x/C and 8-fold larger catalytic mass-based activity than commercial Ir blacks. The electrochemical durability of Ir-ND/ATO at a constant current density for 15 h surpassed that of the reference catalysts. For the $IrNi_x$@IrO_x/ATO, electrochemical stability in constant current and duty-cycling mode showed negligible degradation during a 20 h stability test unlike various Ir−oxide benchmark materials.[34] However, the physical origin of the experimentally observed enhanced electrocatalytic stability of the active IrO_x nanoparticle catalysts when dispersed on metal−oxide supports has not been clarified yet and would greatly advance our knowledge-driven design of oxygen evolution catalysts. This report sets out to address this and provides first evidence that metal/metal−oxide support interactions (MMOSI) appear to play a role in the performance of Ir acid water splitting catalysts.

The MMOSI presented here are related to previously reported metal−support interaction (MSI) effects, which are electronic interactions between the metallic portion of an active phase of a catalyst and its supporting material.[35−39] For instance, Ramani et al. reported $Ta_{0.3}Ti_{0.7}O_2$ as catalysts support for oxygen reduction reaction (ORR) in fuel cells.[40,41] After accelerated durability tests, the loss in voltage at a current density of 0.4 A cm^{-2} of 20% Pt/$Ta_{0.3}Ti_{0.7}O_2$ was 23 mV, which was 14-fold lower than that of 46% Pt/C (330 mV) commercially sourced catalyst (TKK). The enhanced durability was attributed to the MSI effect between the $Ta_{0.3}Ti_{0.7}O_2$ support and platinum nanoparticles, which results in a decrease of the d-band vacancy of platinum due to electron donation from the support to the platinum atoms. Hwang and co-worker reported that Pt/$Ta_{0.3}Ti_{0.7}O_2$ is a highly stable ORR catalyst. After 5000 potential cycles, the ORR activity of Pt/$Ta_{0.3}Ti_{0.7}O_2$ degraded only 8% as compared to its initial state, whereas Pt/C degraded up to 50%. This was attributed to the interaction between Pt and the oxide preventing Pt nanoparticles from agglomeration.[42,43] This is based on the novel nanostructured $Ti_{0.7}Mo_{0.3}O_2$ support with "electronic transfer mechanism" from $Ti_{0.7}Mo_{0.3}O_2$ to Pt that can modify the surface electronic structure of Pt, owing to a shift in the d-band center of the surface Pt atoms. However, only these few works investigated the correlation between MSI effect and stability, and these are restricted to Pt catalysts for ORR in the field of fuel cells.

In this study, we extended our previous investigations, now focusing on the role of redox-active metal−oxide supports for the redox stability of Ir OER nanoparticle electrocatalysts. Metallic Ir nanoparticles were synthesized, supported on high-surface-area mesoporous ATO, and then electrochemically oxidized. The electrocatalytic stability of IrO_x/ATO was investigated and correlated with its electronic structure using X-ray photoelectron spectroscopy (XPS), X-ray absorption near-edge structure (XANES), and extended X-ray absorption fine structure (EXAFS). Transmission electron microscopy (TEM), X-ray diffraction (XRD), and ICP-OES provided additional insights into the physical properties before and after stability tests. On the basis of these results, we provide evidence for a possibly more important active role of metal−oxide supports in stabilizing oxidized metal particles in electrochemical environments. Our insights may aid the preparation of improved practical OER water splitting catalysts.

2. EXPERIMENTAL SECTION

2.1. Preparation of Sb-Doped SnO_2 (ATO) Support. Antimony-doped tin oxide (ATO) with high surface area was synthesized by the methods reported previously.[32] In short, 1.28 g of tetradecylamine ($CH_3(CH_2)_{13}NH_2$, 95%, Sigma-Aldrich) was added to 225 mL of ethanol solution (C_2H_5OH 65 mL, DI water 160 mL) and mixed for 3 h at room temperature. A 4.794 g amount of tin tetrachloride ($SnCl_4$, 99.995%, Sigma-Aldrich) and 0.48 g of antimony(III) acetate ($(CH_3CO_2)_3Sb$, 99.99%, Sigma-Aldrich) were dissolved in 20 mL of ethanol followed by adding into the prepared tetradecylamine (TDA) solution. After stirring for 1 h, the mixture was added dropwise to 200 mL of ammonium hydroxide solution (1.5 mmol L^{-1}). The resulting solution was refluxed for 72 h at 80 °C without stirring and then cooled down to room temperature. The white-yellow precipitate was separated from the solution by centrifugation (8200 rpm, 15 min), and then washing was repeated 5 times with water. The as-prepared wet sample was transferred to a glass-lined stainless-steel autoclave (ROTH) and hydrothermally treated at 120 °C for 24 h. To remove the excess surfactant, product was centrifuged and washed with 40 mL of ethanol solution (C_2H_5OH 20 mL; DI water 20 mL) 5 times. Produced bright yellow powder was dried in a freeze dryer and then calcined in air at 400 °C for 3 h. Detailed synthesis mechanisms are shown in the Supporting Information (SI).

2.2. Preparation of Ir/ATO. For synthesis of the ATO-supported Ir nanoparticles, 74 mg of iridium acetate ($Ir(CH_3COO)_3$, Chempur) and 80 mg of sodium hydroxide (NaOH, ≥99%, ROTH) were dissolved in 20 mL of ethylene glycol under vigorous stirring for 30 min. The calculated amount of ATO as support was added to the solution to produce 20 wt % Ir loading on the support and then dispersed using sonication for 20 min. The resulting suspension was stirred for 15 min under nitrogen flow followed by reflux at 160 °C for 30 min. The reaction mixture was rapidly cooled down to room temperature. Stirring was continued for another 24 h. Next, Ir/ATO powder in the solution was separated by centrifugation (8200 rpm, 15 min) and washed several times with ultrapure water. The collected Ir/ATO slurry was dried in a freeze dryer (−10 °C and ∼1 mbar overnight). The dry powder was thermally treated to remove remains of organic substances at 250 °C in N_2 atmosphere for 2 h. For comparison, carbon black (Vulcan XC-72R, Cabot, 235 m^2 g^{-1}) and commercial ATO (SnO_2/Sb_2O_5, ≥99.5%, Sigma-Aldrich, 47 m^2 g^{-1}) were used to support Ir nanoparticles based on the same protocol described above.

2.3. Materials Characterization. *Transmission Electron Microscopy (TEM).* High-resolution transmission electron microscopy (HR-TEM) was carried out to determine the size and distribution of iridium nanoparticles by using FEI TECNAI G^2 20 S-TWIN equipped with LaB_6 cathode and GATAN MS794 P CCD camera. The micrographs were obtained at an acceleration voltage of 200 kV. The electrocatalysts were dispersed in a 1:1 mixture of ethanol and deionized water (DI water), then dropped onto the carbon-coated copper grids, and finally dried at 50 °C in a convection oven.

Scanning Transmission Electron Microscopy Coupled to Energy-Dispersive X-ray Spectroscopy (STEM-EDX). The local chemical composition and microstructure of IrO_x/ATO after electrochemical oxidation step was investigated by analytical electron microscopy by using a double-Cs-corrected JEOL JEM-ARM200CF scanning transmission electron microscope with a cold field emission gun (FEG). The instruments were operated at 200 kV. EDX maps were recorded by using a Silicon Drift EDX detector. The sample was dispersed in

DOI: 10.1021/jacs.6b07199
J. Am. Chem. Soc. 2016, 138, 12552−12563

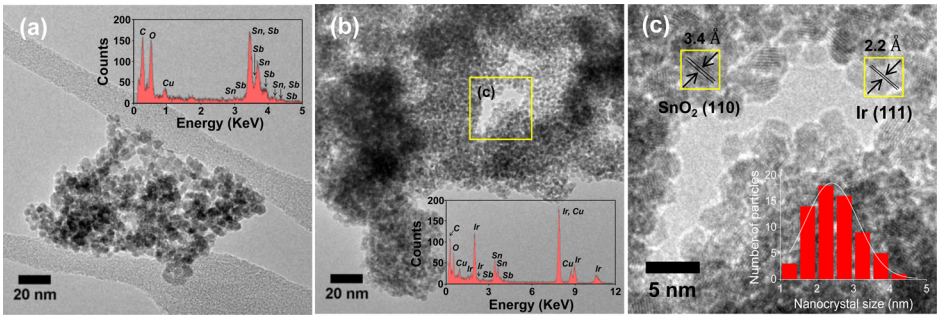

Figure 1. Low-resolution TEM images of as-prepared (a) antimony-doped tin oxide (ATO) with high surface area (inset, EDX pattern of ATO) and (b) Ir nanoparticles supported on ATO (inset, EDX pattern of Ir/ATO). (c) High-resolution TEM image of Ir nanoparticles supported on ATO. (Insets) Corresponding lattice fringes of SnO_2 (110), Ir (111), and nanoparticle size distribution.

ethanol and drop deposited onto holey carbon-coated copper support grids.

Inductively Coupled Plasma Optical Emission Spectroscopy (ICP-OES). ICP-OES analysis was performed to determine the Ir loading on the different supports and to quantity of Ir dissolution during the stability test with a 715-ES-inductively coupled plasma (ICP) analysis system (Varian). The concentrations of Ir-standard solution were 1, 2, 4, and 6 ppm.

X-ray Diffraction (XRD). Powder XRD profiles were measured in Bragg−Brentano geometry using a D8 Advanced Bruker-AXS diffractometer (Cu Kα radiation) to confirm the presence of antimony-doped tin oxide and iridium. Diffraction peaks were recorded in the range 2θ = 20−95° with an increment of 0.05°, a measuring time of 5 s per step, and a sample rotation rate of 15 rpm.

X-ray Absorption Spectroscopy (XAS). XANES/EXAFS experiments were carried out at the 7T-WLS-1 mySpot beamline in BESSY II of the Helmholtz Zentrum Berlin (HZB). The measurements were performed at the L_{III} edge of Ir; the incident beam having a circular shape with a diameter of ca. 300 μs was generated using a Si(111) monochromator. This beamline provides X-ray energies in the range of 8−15 keV. Iridium(IV) oxide (IrO_2, Premion, 99.99%, Alfa Aesar) calcined at 700 °C overnight in air and iridium(III) chloride ($IrCl_3$, 99.8%, Sigma-Aldrich) were used as reference materials for Ir L_{III}-edge measurement. The results were normalized using the program Athena with a linear pre-edge and polynomial postedge background subtracted from the raw $\ln(I_t/I_0)$ data.[44] The k-space range was 2−12 Å^{-1}, and the EXAFS data were obtained by performing a Fourier transform on the r space, which was set at 0.3−7 Å. All XAS spectra were calibrated with Ir foil. To prepare the electrode, as-synthesized electrocatalysts were coated on a carbon paper (10 × 50 mm) and then electrochemically oxidized using cyclic voltammetry (500 mV s^{-1}, 0.05−1.5 V_{RHE}, 50 cycles) in 0.05 M H_2SO_4.

X-ray Photoelectron Spectroscopy (XPS). X-ray photoelectron spectroscopy (XPS) was performed at the ISISS beamline of the BESSY II synchrotron facility in Helmholtz Zentrum Berlin (HZB). The experimental setup was described in detail.[45,46] As-synthesized electrocatalysts were coated on glassy carbon using the drop-coating technique and then underwent an electrochemical treatment. Prepared samples were mounted onto a sapphire holder and introduced into the spectrometer. XPS experiments were carried out at room temperature in ultrahigh vacuum (UHV). For depth profiling, the Ir 4f spectrum was recorded using the kinetic energies of the photoelectrons of 210 and 550 eV.

Differential Electrochemical Mass Spectrometry (DEMS). DEMS was used to record the evolved O_2 simultaneously to the current in cyclic voltammetry. A home-designed dual thin layer electrochemical flow cell was used, in which the electrolyte is under continuous flow (5 μL s^{-1}). O_2 evolved at the electrode in the flow cell was detected using a PrismaTM quadrupole mass spectrometer (QMS 200, Pfeiffer-Vacuum) with two turbomolecular pumps (HiPace 80) operating under 10^{-6} mbar. The electrolyte was separated from the chamber by a 150 μm thick hydrophobic PTFE membrane (Cat. No. PF-003HS for Cobetter porous size 30 nm). Further details can be found in the Supporting Information (SI).

2.4. Electrochemical Analysis of IrO_x/ATO and Durability Studies. Electrochemical analysis was conducted in a conventional three-electrode electrochemical cell using 0.05 M H_2SO_4 saturated with nitrogen (N_2). A glassy carbon electrode (RDE, Pine Research instrument, 0.196 cm^2) with a thin film of prepared catalyst was used as the working electrode, whereas a platinum mesh and mercury/mercury(II) sulfate (MMS, Hg/Hg_2SO_4) electrode were used as the counter and reference electrodes, respectively.[47] The catalyst ink was prepared by blending 5.0 mg of electrocatalysts powder into a solvent of isopropyl alcohol (2.49 mL, ≥99.7%, Sigma-Aldrich), ultrapure water (2.49 mL), and 5 wt % Nafion ionomer (20 μL, Nafion 117 solution, Sigma-Aldrich). The prepared ink was deposited onto the glassy carbon electrode (10.2 μg_{Ir} cm^{-2}) followed by drying in a convection oven at 50 °C.

Prior to electrochemical analysis, the surface of the synthesized iridium nanoparticles was oxidized using a potential sweep between 0.05 and 1.5 V_{RHE} for 50 cycles at a scan rate of 500 mV s^{-1}.[48] The electrochemical catalytic activity of synthesized catalysts was recorded during cyclic sweep voltammetry between +1.0 and +2.0 V with a scan rate of 5 mV s^{-1} under electrode rotation of 1600 rpm. The stability of electrocatalysts was tested by using a chronopotentiometric experiment, in which the current density was held at 1 and 10 mA cm^{-2} for 15 and 1.5 h, respectively, while the potential was recorded. Impedance analyses were carried out at +1.7 V_{RHE} in the frequency range from 1 Hz to 100 kHz before and after the galvanostatic stability test.

3. RESULTS

3.1. Morphology and Structure of ATO-Supported Ir Nanoparticles. The structures of the synthesized antimony-doped tin oxide (ATO) and Ir nanoparticles supported on ATO samples were characterized by TEM measurements at low and higher resolution. Figure 1a shows that ATO nanoparticles interconnect each other and have a particle size of approximately 3−5 nm. The corresponding energy-disperse X-ray (EDX) spectroscopy (Figure 1a, inset) indicated that the material was composed of Sn, Sb, and O.

Ir nanoparticles were subsequently deposited onto the ATO support using the well-known polyol method. This method is typically used for reducing precious metal precursor with ethylene glycol simultaneously acting as solvent, reducing agent, and stabilizer.[49] Figure 1b displays the TEM image of the as-prepared Ir/ATO catalyst−support couple, displaying spherical Ir nanoparticles homogeneously distributed on the ATO support. The EDX pattern (Figure 1b, inset) of Ir/ATO shows the peaks of Ir, Sn, and Sb elements, confirming the presence of Ir nanoparticles on the ATO support. The higher resolution TEM image (Figure 1c) clearly shows that Ir

DOI: 10.1021/jacs.6b07199
J. Am. Chem. Soc. 2016, 138, 12552−12563

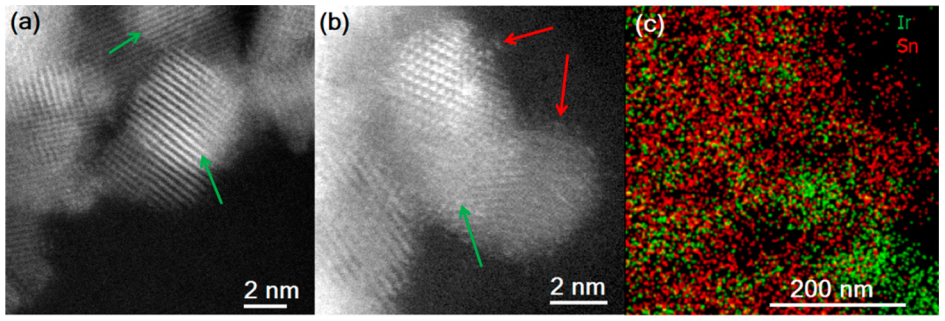

Figure 2. Electron microscopy images of the IrO_x/ATO sample after electrochemical activation. (a, b) Representative high-resolution HAADF images, and (c) EDX mapping shows a homogeneous Ir distribution on the ATO support (green, Ir; red, Sn).

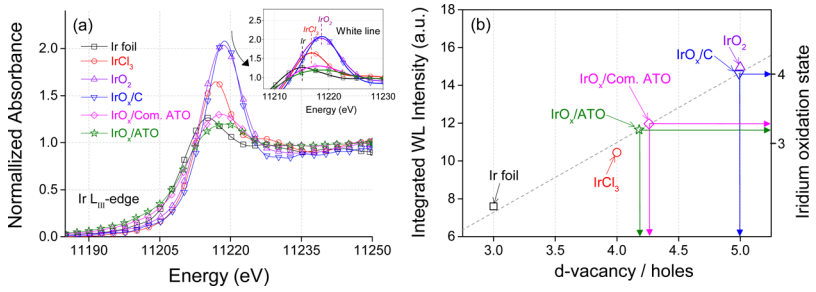

Figure 3. Ir L_{III}-edge XANES data of electrochemically activated (oxidized) IrO_x/C, IrO_x/Com. ATO, IrO_x/ATO, and reference materials: (a) normalized XANES spectra (inset shows a magnified region of Ir L_{III}-edge XANES white line) and (b) integrated white-line versus d vacancy and Ir oxidation state for the reference materials with IrO_x/C, IrO_x/Com. ATO, and IrO_x/ATO indicated. It was assumed that Ir foil ($5d^7\ 6s^2$), $IrCl_3$ ($5d^6\ 6s^0$), and precalcined commercial IrO_2 ($5d^5\ 6s^0$) as the reference materials have d vacancies of 3, 4, and 5, respectively. For the Ir oxidation state, $IrCl_3$ and precalcined commercial IrO_2 were assumed +3 and +4, respectively.

nanoparticles with a diameter of about 3 nm were well supported on ATO. Moreover, the insets demonstrate the good crystallinity of ATO judging from the well-defined fringes of 3.4 Å corresponding to the spacing of the (110) plane of SnO_2. The lattice spacing of 2.2 Å was indexed as (111) of the fcc Ir, which indicated that Ir nanoparticles with good crystallinity were adhered to the ATO support. This result was further supported by the XRD measurement, as shown in Figure S1. The diffraction peaks at around $2\theta = 26.6°$, 33.9°, and 51.8° are indexed to the (110), (101), and (211) planes of the tetragonal rutile-type SnO_2 structure (JCPDS card no. 21-1250).[32] The iridium diffraction peak at 40.6° was indexed to the (111) reflection of the fcc Ir metal (JCPDS card no. 87-0715), indicating the formation of crystalline Ir nanoparticles in Ir/ATO.[33] In order to determine the Ir loading on the ATO support, inductively coupled plasma optical emission spectroscopy (ICP-OES) analysis was performed indicating 17.3 wt % Ir. This value is in reasonable agreement with the nominal Ir concentration (20 wt %), which suggests that most of the Ir salt was reduced and loaded on ATO. In addition to the synthesized ATO support, iridium nanoparticles were also supported on a commercial ATO ("Com. ATO") and a carbon black support; these Ir catalysts were used for comparison and performance reference. The TEM image in Figure S2a shows that the Ir nanoparticles were uniformly distributed over the carbon support. The average size of Ir nanoparticle was 2.5 nm. Ir nanoparticles on Com. ATO (Figure S2b) were agglomerated and poorly dispersed, because the surface area of a Com. ATO (47 $m^2\ g^{-1}$) was much lower than those of the synthesized ATO (263 $m^2\ g^{-1}$) and the carbon black (235 $m^2\ g^{-1}$). In addition, the corresponding low-magnification TEM images are shown in Figure S3.

3.2. Electrochemically Oxidized ATO-Supported IrO_x Nanoparticles. We subjected the as-synthesized supported Ir catalysts from section 3.1 to a cyclic voltammetric potential sweep protocol ranging from +0.05 to +1.5 V_{RHE}.[33,34] This electrochemical treatment transformed the Ir particle into oxidized Ir particles and served as a standardized activation for the electrocatalysts prior the electrochemical water oxidation (oxygen evolution) reaction.

To understand the detailed morphology of the oxidized IrO_x nanoparticles on ATO support, high-angle annular dark field (HAADF) STEM and EDX element mapping were performed. Figure 2 shows high-resolution HAADF images of the IrO_x/ATO sample after electrochemical activation measured at low electron beam dose (1.7 pA/cm^2). ATO particle surfaces are decorated with atomic clusters which can be attributed to IrO_xH_y amorphous species (marked with red arrows in the Figure 2b). Moreover, some ATO particles exhibit irregular Z-contrast of lattice fringes with some highlighted regions (marked with green arrows in the Figure 2a and 2b). These high-Z-contrast regions are most probably due to rutile IrO_x nanoclusters. As shown in Figure 2c, EDX map on submicrometer scale shows a homogeneous distribution of Ir and Sn which is in line with the HAADF observation. In addition, HAADF images measured at high electron beam dose (17 pA/cm^2) results in formation of homogeneously distributed Ir metallic particles on ATO surface due to beam-induced reduction (Figure S4).

3.3. Local Atomic and Electronic Structure of Electrochemically Oxidized OER Electrocatalysts. In order to analyze the Ir oxidation state, we characterized the electronic structure of the electrochemically oxidized supported IrO_x OER

DOI: 10.1021/jacs.6b07199
J. Am. Chem. Soc. 2016, 138, 12552−12563

electrocatalysts using X-ray absorption spectroscopy (XAS) and X-ray photoelectron spectroscopy (XPS).

Figure 3a shows the Ir L_{III}-edge X-ray absorption near-edge spectroscopy (XANES) region of the IrO_x/ATO catalyst compared to IrO_x/C and IrO_x/Com. ATO. In addition, three commercial Ir compounds (Ir foil, $IrCl_3$, and IrO_2) as references were measured under the same condition. The absorption at 11 215 eV corresponds to the $2p_{3/2}$ to 5d electronic transition of Ir; the pronounced absorption edge is historically referred to the white line.[50,51] Although 2p → 6s transition is also electric dipole allowed, this transition has been disregarded because the matrix element of this transition is much smaller than that of the transitions to d states, $\langle 6s|\mu|2p\rangle \ll \langle 5d|\mu|2p\rangle$.[52] The $2p_{3/2}$ to 5d white line generally provides information about the number of empty d holes (d vacancy) in transition metal catalysts.[53] As the d vacancy increases, the peak position of the white line shifts toward higher energies and the integrated intensity of the white line monotonically increases.[54] Therefore, the peak position of white-line feature in Figure 3a is an indicator of electron vacancies in the 5d orbitals of Ir atoms, which decrease in the order IrO_x/C ≈ IrO_2 ≫ IrO_x/Com. ATO ≈ IrO_x/ATO > Ir foil (inset in Figure 3a).

To quantitatively elucidate how the nature of the support affects the d vacancy and Ir oxidation state, we carried out a deconvolution analysis of the integrated white line using arctangent and Lorentzian functions, as shown in Figure S5.[55] An arctangent function subtracted from the experimental data yielded the contribution for the white-line feature. The integral area of the so-calculated white line is proportional to the local density of unoccupied final states.[54] Figure 3b shows the integrated white line as a function of d vacancy and oxidation state of samples and reference materials. This graph clearly evidence that the d vacancy of the oxide-supported IrO_x is significantly approaching 4 holes, which is lower than that of bulk crystalline IrO_2 (5 holes). For the carbon-supported IrO_x, however, the d vacancy is essentially 5 holes. In terms of average Ir oxidation states, IrO_x/Com. ATO, IrO_x/ATO, and IrO_x/C were +3.3, +3.2, and +4.0, respectively (see summarized result in Table 1).

Table 1. Results of the White-Line Area Analysis in Ir L_{III} XANES Spectra

sample	electronic structure	d vacancy (holes)	$I_{L_{III}}$ (numeric)	Ir oxidation state
Ir foil	$5d^7\ 6s^2$ (Ir)	3	7.6	
$IrCl_3$	$5d^6\ 6s^0$ (Ir^{3+})	4	10.4	+3.0
IrO_2	$5d^5\ 6s^0$ (Ir^{4+})	5	15.0	+4.0
IrO_x/C	$5d^5$ (Ir^{4+})	5	14.6	+4.0
IrO_x/Com. ATO	$5d^{5.7}$ ($Ir^{3.3+}$)	4.3	12.0	+3.3
IrO_x/ATO	$5d^{5.8}$ ($Ir^{3.2+}$)	4.2	11.7	+3.2

To further corroborate the observed discrepancies with regard to the Ir oxidation state of oxide-supported IrO_x nanoparticles, we assessed the Ir−O bond distances as a function of the Ir oxidation states of the IrO_x catalysts. It is known that the oxidation state of metal−oxides can affect their metal−oxygen bond distance.[56] The metal−oxygen bond distance of well-defined, crystalline metal−oxides could, in principle, be obtained by standard XRD techniques. However, it is not easy to accurately measure metal−oxygen bond distance due to the low X-ray scattering factor and the difficulty of sample preparation after the electrochemical activation protocol.[56] Hence, extended X-ray absorption fine structure spectroscopy (EXAFS) was used to obtain local structural information on Ir coordination in the IrO_x/C, IrO_x/Com. ATO, and IrO_x/ATO catalysts and reference IrO_2, see Figure 4.

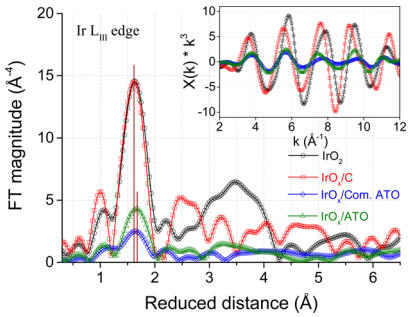

Figure 4. Fourier transform (FT) of extended X-ray absorption fine structure (EXAFS) spectra at the Ir L_{III} edge collected for IrO_x/C, IrO_x/Com. ATO, and IrO_x/ATO catalysts with the reference IrO_2. (Inset) Corresponding k^3-weighted EXAFS spectra.

The inset of Figure 4 shows the k^3-weighted EXAFS spectra of Ir L_{III} edge. Characteristic oscillations are visible below the noise level up to 12 Å^{-1}, indicating good data quality for both the XANES and the EXAFS spectra.[57,58]

The corresponding Fourier transforms (FT) of k^3-weighted EXAFS oscillations at the Ir L_{III} edge are shown in Figure 4. The resulting peaks are related to coordination shells of Ir (Ir−O and Ir−Ir), caused by the interference between the electronic back scatterings from Ir to O and Ir neighbors.[56,57] The main peaks around 1.6 Å reduced distance represent the Ir−O bond, caused by the electron backscattering of the octahedral oxygen environment around the central Ir atom. There are also smaller peaks between 2.4 and 3.5 Å reduced distance representing the contribution of Ir−Ir coordination shells to the EXAFS oscillations.[56,57] Inspection of the Ir−O peak positions of the oxide-supported IrO_x/ATO and IrO_x/Com. ATO catalysts revealed that their Ir−O distances were shifted to larger values compared to the IrO_x/C and calcined crystalline IrO_2 catalysts in agreement with a lower average redox state of Ir.

Now we turn to an investigation how the Ir oxide layer thickness depends on the nature of the support. The oxide thickness of OER electrocatalysts has been previously hypothesized to control the activity and stability of the active catalyst phase.[59] We will test this hypothesis using the oxide- and carbon-supported IrO_x catalyst. In practice, starting from pure metal surfaces and exposing them to anodic polarizations inside the OER potential region, electrochemically induced catalytically active RuO_x layers are typically 4-times thicker than those of the IrO_x layer at the same applied polarization of +1.45 V_{RHE}. This was thought to be in causal relation with the improved catalytic water oxidation activity and reduced stability of RuO_x compared to IrO_x.[59,60]

Following this argument we hypothesize that the lower oxidizability of metallic Ir may account for improved stability. To test this hypothesis, we carried out synchrotron-based depth-resolved X-ray photoelectron spectroscopy (XPS) to gain insight into the support-dependent Ir oxide thickness of all electrocatalysts (Figure 5). The applied 210 and 550 eV photoelectron kinetic energy corresponds to 5.2 and 9.3 Å inelastic mean free path, based on the TPP-2M predictive formula of Tanuma et al.[61] The high-resolution Ir 4f spectra

DOI: 10.1021/jacs.6b07199
J. Am. Chem. Soc. 2016, 138, 12552−12563

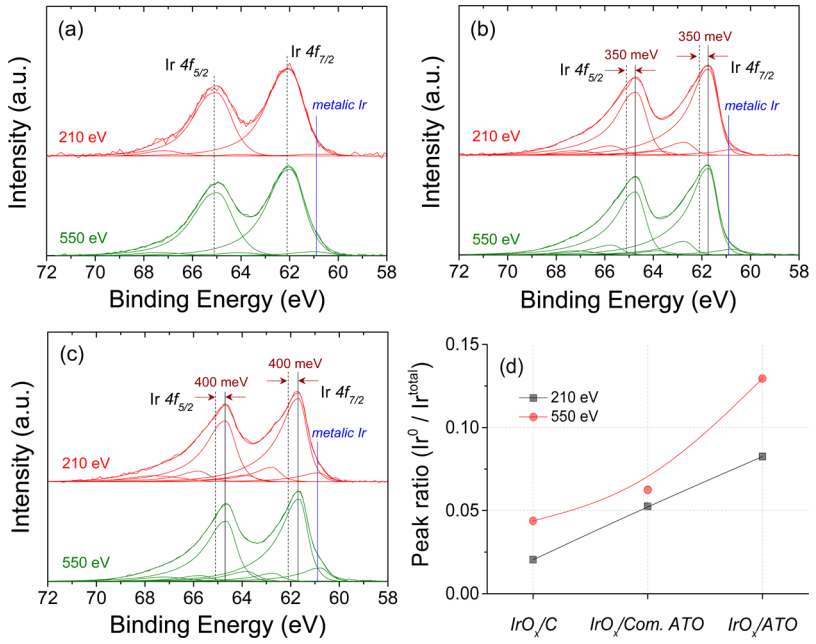

Figure 5. Depth-resolved Ir 4f XPS spectra of electrochemically activated (a) IrO_x/C, (b) IrO_x/Com. ATO, and (c) IrO_x/ATO. Top to bottom spectra were measured at photoelectron kinetic energies of 210 and 550 eV. Blue lines indicate the peak position of metallic Ir, and dashed vertical lines indicate the IrO_x/C peak position for comparison. (d) Peak area ratio of Ir(0) to Ir(total) with different kinetic energies at the photoelectrons of 210 and 550 eV.

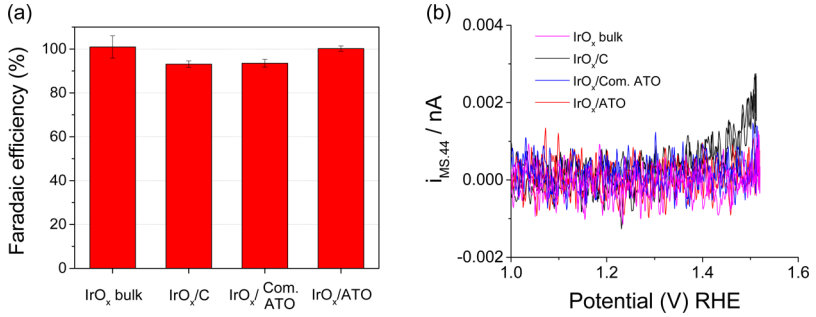

Figure 6. (a) Faradaic efficiency of electrochemically oxidized IrO_x/ATO catalyst, and (b) ionic current for m/z = 44 (CO_2) of electrocatalysts (pink, bulk IrO_x; black, IrO_x/C; blue, IrO_x/Com. ATO; red, IrO_x/ATO).

show the Ir $4f_{7/2}$ and Ir $4f_{5/2}$ spin−orbit doublet, appearing with somewhat different shape and at different binding energy with the samples. The metallic Ir peak appears at 60.9 eV and is indicated as a vertical blue line.[62] To account for the changing line shape, we performed a curve-fitting procedure. For IrO_x/C, the Ir $4f_{7/2}$ binding energy shows up at ∼62.1 eV, and the metallic component was almost absent at both kinetic energies (KE) of 210 and 550 eV, indicating that Ir atoms in the surface layer were completely oxidized. In comparison, the depth profiles of IrO_x/ATO and IrO_x/Com. ATO showed metallic Ir components at both KE clearly. Figure 5d reports the proportion of Ir(0) to the total signal intensity and demonstrates a decreasing extent of Ir oxidation in the order of IrO_x/C > IrO_x/Com. ATO > IrO_x/ATO. It is worth noting that the Ir 4f line shape of oxidized Ir is very different when supported on a carbon or on the two types of ATOs. The line shape and binding energy of ATO-supported IrO_x is more reminiscent of thermally prepared IrO_2, whereas the Ir 4f of IrO_x/C is more upshifted and less asymmetric.[63] The highest binding energy Ir $4f_{7/2}$ species between 62 and 63 eV likely signals the presence of Ir^{3+} species, as discussed recently by Pfeifer et al. based on a combined high-resolution XPS and DFT study.[62] The presence of small Ir^{3+} and metallic Ir contributions corroborates our earlier findings regarding the lower average Ir oxidation state in the oxide-supported IrO_x nanoparticles compared to the carbon-supported IrO_x nanoparticles.

3.4. DEMS Experiments of Electrochemically Oxidized Electrocatalysts in Oxygen Evolution Reaction. In order to obtain the faradaic efficiency of electrocatalysts under OER, differential electrochemical mass spectrometry (DEMS) was used with a flow-cell system, and details are described in the Supporting Information (SI). The typical cyclic voltammograms (CV) and mass spectrometric cyclic voltammograms (MSCV) of OER were measured, as shown in Figure S6. Simultaneously to the electrochemical current, the mass spectrometric signal for oxygen (m/z = 32) and carbon dioxide (m/z = 44) were recorded. Using these results, the faradaic efficiency was calculated, which are shown in Figure 6a. IrO_x/ATO and bulk IrO_x showed 100% faradaic efficiency for OER, demonstrating the high selectivity toward water oxidation reaction. However, IrO_x/C has about 93% efficiency due to the

DOI: 10.1021/jacs.6b07199
J. Am. Chem. Soc. 2016, 138, 12552−12563

carbon oxidation during OER measurement. Figure S7 shows the ionic current signal of carbon dioxide obtained in DEMS measurements, and the result of IrO_x/C exhibited an oxidation of carbon support material from 1.45 V_{RHE} resulting in the decrease of faradaic efficiency. IrO_x/Com. ATO showed 94% faradaic efficiency, which is evidenced the oxidative instability of the commercial ATO support and would explain the low oxidation state of Ir nanoparticles onto the Com. ATO support.

3.5. Galvanostatic Stability of Electrochemically Oxidized Electrocatalysts. The electrochemical stability of the IrO_x/ATO OER catalyst was tested together with the reference materials at constant water oxidation current densities for 15 h in strongly acidic conditions (pH 1).

As shown in Figure 7, all measured electrode potentials gradually increased, suggesting slow catalytic activity degradation. For IrO_x/C and IrO_x/Com. ATO, the electrode potential sharply rose above 1.9 V_{RHE} after 9 and 13 h, respectively, and then leveled off. The overall voltage stability of the electrocatalysts increased in the order IrO_x/C < IrO_x/Com. ATO < IrO_x/ATO. In order to evaluate the stability in higher current density condition, 10 mA cm^{-2} was applied. As shown in Figure S8, even though their electrode potentials were initially similar, the measured potential during the stability test sharply increased to 2.4 V_{RHE} after 15 min and 1.2 h for IrO_x/C and IrO_x/Com. ATO, respectively, whereas the IrO_x/ATO catalyst showed negligible degradation. This result indicates that ATO-supported electrocatalysts exhibited a clearly more stable behavior than the carbon-supported IrO_x.

To get quantitative insight into the absolute Ir metal dissolution during the galvanostatic stability test, the concentration of dissolved Ir in the electrolyte was monitored using ICP-OES. The IrO_x/C catalyst showed a considerable Ir mass loss of about 71.6% of the initial Ir loading. For the IrO_x/Com. ATO catalyst 61.7% Ir mass-based dissolution was observed, while only 21.4% Ir mass loss occurred for the IrO_x/ATO material. Although the ICP experiment provides important quantitative information about the Ir dissolution during the stability test, it does not fully explain the underlying degradation during chronopotentiometry. Therefore, a complementary TEM-based EDX analysis was carried out to measure the residual Ir amount of each catalyst after the stability test. The results are shown in Figure S9, and the remaining Ir percent by mass were 0.7, 2.5, and 11.3 wt % for IrO_x/C, IrO_x/Com. ATO, and IrO_x/ATO, respectively. The calculated Ir mass losses of each catalyst were 97.1%, 84.2%, and 28.3% of their initial Ir loading. The differences between EDX and ICP results can be attributed to the detachment of IrO_x nanoparticles; this is because detached nanoparticles in the electrolyte go undetected in the entire ICP measurements. As shown in Figure S10, the proportion of detached IrO_x in IrO_x/C was about 26% of the initial Ir loading. The IrO_x/Com. ATO

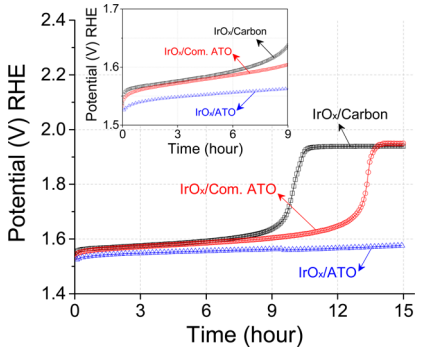

Figure 7. Constant current stability test of IrO_x/ATO electrocatalysts for OER in comparison to reference catalysts measured under identical conditions. The result of reference catalysts (IrO_x/C and IrO_x/Com. ATO) was similar to our previous report.[34] Measurement condition: 25 °C, 0.05 M H_2SO_4, 1600 rpm, 1 mA cm^{-2}, N_2-purged condition. Test time: 15 h. Ir loading: 10.2 μg_{Ir} cm^{-2}. (Inset) Magnification over the 0–9 h region.

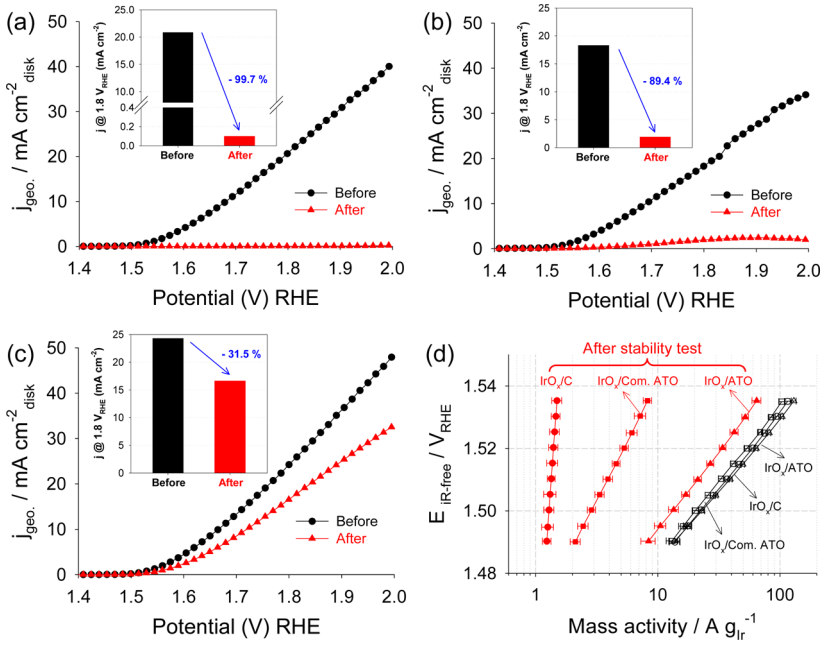

Figure 8. Electrocatalytic OER polarization curve before and after stability test: (a) IrO_x/C, (b) IrO_x/Com. ATO, and (c) IrO_x/ATO. (Inset) Corresponding geometric activity at 1.8 V_{RHE}. (d) *iR*-corrected Tafel plots of electrocatalysts before and after the stability test. All measurements were performed in N_2-purged 0.05 M H_2SO_4. Catalysts loading: 10.2 μg_{Ir} cm^{-2}. Scan rate: 5 mV s^{-1}.

DOI: 10.1021/jacs.6b07199
J. Am. Chem. Soc. 2016, 138, 12552–12563

showed Ir detachment of 23%, whereas for IrO_x/ATO it was merely 6.9%.

3.6. Electrocatalytic OER Performance and Charge-Transfer Kinetics before and after Stability Testing. To evaluate the impact of the galvanostatic stability tests on the catalytic performance of the IrO_x OER nanoparticle catalysts, OER polarization curves before (black) and after (red) stability testing were recorded and are compared in Figure 8a–c.

The oxygen evolution commenced in the kinetically controlled regime at about 1.5 V_{RHE} and exponentially increased as the cell voltage rose to 1.6 V_{RHE}.[64] Above 1.6 V_{RHE}, the ohmic electrolyte resistance became dominant.[64] Prior to stability testing, the OER activities of IrO_x/ATO, IrO_x/C, and IrO_x/Com. ATO at 1.8 V_{RHE} were very similar (black symbols and bars in Figure 8a–d), as the OER activity at this positive potential is largely controlled by ohmic resistances, which were found to be almost identical for the initial catalysts (see impedance analysis below). Thus, the reduced oxidation state of the oxide-supported IrO_x particles was not detrimental to their activity. After the stability test, however, IrO_x/C showed a drastic performance decline by 99.7% at 1.8 V_{RHE}. In contrast, there was a 89.4% drop for IrO_x/Com. ATO and a 31.6% drop for the IrO_x/ATO catalyst (red symbols in Figure 8). Figure S11 and Figure 8d compare the catalytic activities of all catalysts using the widely popular and technically relevant Ir-mass basis at lower overpotentials. The data shows that there is a correlation between improved performance stability and resistance to oxidation due to the use of ATO as catalyst support. In particular, Figure 8d shows the corresponding Tafel plots before and after the stability test. The Tafel slope is generally an inherent property of the catalyst, which may point to the rate-limiting step of the reaction mechanism.[65,66] Prior to stability testing, the Tafel slope for all samples was in the range of 56.8–59.4 mV dec^{-1}, close to the theoretical value of 60 mV dec^{-1}.[63,67,68] After the stability test, the Tafel slope of IrO_x/ATO maintained a low 61.7 mV dec^{-1}, reiterating its stability, followed by IrO_x/Com. ATO catalyst with 87.4 mV dec^{-1} and by IrO_x/C with 537.0 mV dec^{-1}, which indicates an almost complete loss of activity.

To analyze the interfacial charge-transfer kinetics, impedance analysis, presented in Figure 9, was performed before and after the stability test. All impedance experiments were carried out at +1.7 V_{RHE} in the frequency range from 1 Hz to 100 kHz. All ohmic resistances remained very similar in magnitude before and after stability testing. This observation is important as it rules out variations in the electronic conductivity of the catalyst/support materials as the origin of the chemical reactivity patterns. All kinetic charge-transfer resistances ranged around 35 Ω prior to stability testing yet sharply increased afterward, displaying a decreasing charge-transfer resistance in the order IrO_x/C > IrO_x/Com. ATO > IrO_x/ATO.

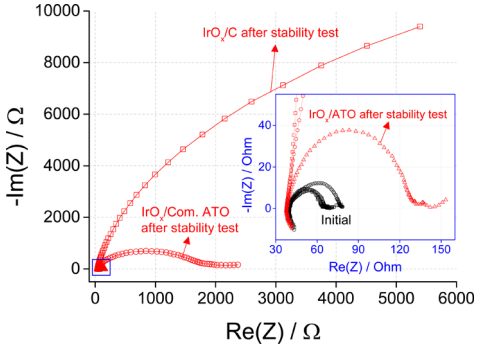

Figure 9. Impedance spectroscopic Nyquist plot of the IrO_x/C, IrO_x/Com. ATO, and IrO_x/ATO catalysts evaluated at +1.7 V_{RHE} before (black) and after (red) the galvanostatic stability test. (Inset) Magnification over the 30–150 Ω region.

To examine the influence of long-term stability on the structure of the electrocatalysts, all samples from the tested electrodes were analyzed by TEM. Figures 10 and S12 show

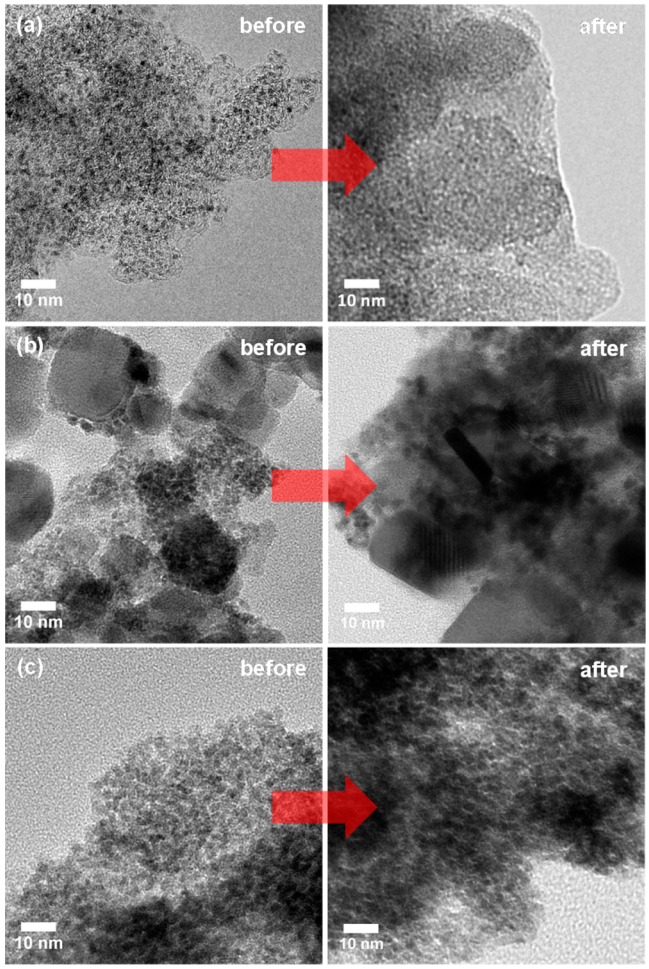

Figure 10. TEM images of IrO_x/C, IrO_x/Com. ATO, and IrO_x/ATO electrocatalysts before and after stability (Chronopotentiometry at 1 mA cm^{-2}, for 15 h).

TEM images of the catalyst particles of IrO_x/C, IrO_x/Com. ATO, and IrO_x/ATO before and after the galvanostatic stability test. After stability testing, Figure 10a confirms a collapsed and corroded carbon structure for IrO_x/C associated with a low density of Ir particles. For IrO_x/Com. ATO (Figures 10b and S12b), Ir nanoparticles extensively coarsened and ripened after the stability test. In contrast, no significant differences between the pristine and the tested IrO_x/ATO catalysts (Figures 10c and S12c) were observed, indicating similar IrO_x particle size before and after the stability test. For the IrO_x/C, the remaining Ir percent by mass onto the carbon support was 0.7 wt %, which was about 3% of the initial Ir loading.

DOI: 10.1021/jacs.6b07199
J. Am. Chem. Soc. 2016, 138, 12552–12563

4. DISCUSSION

DSA-type electrodes containing a second metal−oxide next to IrO_x provided an enhanced stability, which was rationalized by proposing an improved conductivity, bonding improvement, surface morphology, compact microstructure, and solid solution.[10] However, these approaches are restricted to the physical and electrical topic. Hence, the object of this study is to broaden these approaches toward electronic structure effects.

4.1. Electronic Structure Effects Due to Interactions between Metal−Oxide Particles and Their Support (MMOSI). Given the long history of electronic structure effects in oxide-supported metallic nanoparticles used to heterogeneously catalyze gas-phase reactions, we set out to explore whether there is evidence for electronic interactions between oxidic supports and oxidic nanoparticles during electrocatalytic reactions. We chose the electrochemical water oxidation on supported Ir oxide nanoparticles (oxygen evolution reaction, OER) as model system.[35,39,40,42,43,69] To obtain insight in the electronic structure and charge-transfer dynamics, we correlated results from a diverse set of techniques including transmission electron microscopy, X-ray absorption and X-ray photoemission spectroscopies, electrochemical voltammetry, chronoamperometry, potentiometry, and impedance spectroscopy.

Evidence for the presence of electronic interactions between the oxidized IrO_x nanoparticles and their ATO supports was provided by the characteristic X-ray absorption white-line intensity patterns given in Figure 3a. The position and the overall intensity of the white line is used for the determination of the oxidation state.[70] A shift toward higher energy of the main peak indicates an increasing number of vacant d states and oxidation of Ir.[70] While the observed variations in the white-line intensity could in principle be caused by a crystallite size effect, this explanation can be ruled out here, because the dimensions of the Ir particles were very similar based on the presented microscopic data.[71] It is more plausible to attribute the experimental decrease in the white-line intensity of the ATO-supported versus carbon-supported catalysts to an electronic effect, likely an interfacial electron transfer to the Ir centers of the catalytically active nanoparticles, caused by an interaction at the interface of the oxidized IrO_x nanoparticles and their ATO support. In the field of heterogeneous gas-phase catalysis, such interactions have been termed "metal−(oxide) support interactions" (MSI).[39−43,72] In view of the electrochemically oxidized IrO_x nanoparticle surfaces, however, we refer to this phenomenon as metal/metal−oxide support interactions (MMOSI).

In addition to the XAS results, the electronic charge donation from the ATO support to the active IrO_x catalysts is corroborated by the characteristic trend in the Ir oxidation state (Figure 3b). Ir oxidation was evidently impeded on the ATO support yet preceded to completion on the carbon support. In this context, we note that based on our impedance and charge-transfer resistance analysis, variations in the electronic conductivity of the three catalyst−support couples can be ruled out as the origin of the different average Ir oxidation states. As shown in Figure S13, all kinetic charge-transfer resistances were essentially identical for the nanoparticle catalyst/support systems.

The Ir−O bonding distances from our EXAFS analysis provide further independent evidence in favor of our MMOSI hypothesis regarding a change in the electronic structure of oxide-supported versus carbon-supported IrO_x nanoparticles. As shown in Figure 4, the peaks of IrO_x/Com. ATO and IrO_x/ATO were broader and lower than that of IrO_x/C. This result indicates that the oxide-supported catalyst displays a low coordination number, and the increase in the Ir−O bonding distances is consistent with a lower average Ir oxidation state.[56,73]

Finally, we carried out depth-resolved XPS to study the effect of the three supports on the respective Ir oxide thickness for each electrocatalyst, see Figure 5. These results evidenced a reduced effective oxide thickness for the ATO-supported IrO_x particle catalysts as compared to the carbon-supported one. This finding corroborates our hypothesis and is in full agreement with our XANES results of Figure 3, because it indicates a lower degree of surface oxidation of Ir when supported on oxidic materials.

Overall, our results support the existence of an electronic MMOSI effect in oxide-supported oxide nanoparticle systems, in particular in the IrO_x/ATO catalyst−support couple. This effect appears to stabilize Ir atoms of the IrO_x nanoparticles in an average oxidation states clearly below +4 and to be conducive for thinner surface oxide layer thicknesses.

4.2. Role of MMOSI and Support Effects in the Electrochemical Stability of IrO_x Water-Splitting Catalysts. To unravel and deconvolute the roles of support and catalytically active nanoparticles in the electrochemical stability of the supported catalysts, the galvanostatic chronopotentiometric behavior of the IrO_x/ATO catalyst with its lower Ir oxidation state and thinner oxide layer thickness was recorded and compared with that of the two catalysts. The sharp rise in the measured electrode potentials for both the carbon support and the commercial ATO support evidenced a significantly lower performance stability of these catalyst/support couples. The close resemblance of the black and red voltammetric (chronopotentiometric) trajectories in Figure 7, on the other hand, may suggest similar degradation mechanisms. This can be qualitatively rationalized by a Butler−Volmer-type expression according to[74]

$$j_{\mathrm{OER}} = j_0 \cdot A_{\mathrm{IrO}_x} \cdot L_{\mathrm{IrO}_x} \cdot \exp\left(\frac{\alpha F}{RT}\eta\right) \quad (1)$$

where j_{OER} is the experimentally applied (constant) current density [in mA cm_{geo}^{-2}], j_0 is the exchange current density of the OER on IrO_x [in mA cm_{IrOx}^{-2}] and represents the intrinsic catalytic OER activity of a IrO_x surface, A_{IrO_x} is the electrochemical active surface area (ECSA) [in $cm_{\mathrm{IrO}_x}^2\ g_{\mathrm{IrO}_x}^{-1}$], and L_{IrO_x} is the geometric IrO_x electrocatalyst loading [in $g_{\mathrm{IrO}_x}\ cm_{geo}^{-2}$]. The parameter α is the experimental transfer coefficients, η is the kinetic overpotential of the OER, and F, T, and R have their usual meanings. On the basis of this relation, the experimental OER overpotential during a constant-current stability test is expected to decrease linearly with the logarithm of the product of j_0, A_{IrO_x}, and L_{IrO_x}.[74]

The initially gradual and subsequent sharp increase in the electrode overpotential can be understood in terms of a steady drop in available active IrO_x surface area, A_{IrO_x}, attributable to gradual support corrosion degradation, Ostwald particle ripening, or particle coalescence. Support corrosion invariably implies IrO_x particle detachment and a concomitant drop in L_{IrO_x}, thereby contributing to the rise in overpotential.[75] Once the remaining electrochemically accessible IrO_x nanoparticles are no longer able to provide the required interfacial current

DOI: 10.1021/jacs.6b07199
J. Am. Chem. Soc. 2016, 138, 12552−12563

density, surface sites of the collapsed support material must contribute to the catalytic reaction process. Owing to their much smaller intrinsic j_0 values, this results in a further increase in the effective overpotential (eq 1), where the support degradation, in turn, accelerates further. The system now enters a regime of accelerated degradation manifesting itself in a sharp rise in overpotential.

For IrO_x/C, rapid carbon oxidation above 1.5 V_{RHE}, according to $C + H_2O \rightarrow CO_2 + 4H^+ + 4e^-$ (standard electrode potential $\Delta E^0 = +0.207$ V_{RHE}), plausibly accounts for a collapse of the porous carbon structure, resulting in a severe loss of electrochemically accessible IrO_x surface and consequently loss in active area.[75,76] Carbon surface sites with their much smaller exchange current density almost certainly contributed to the oxygen evolution process, evidenced by the dramatic change of the Tafel slope and position. The IrO_x/Com. ATO catalyst shows much better electrochemical stability than the IrO_x/C catalyst, owing to the higher corrosion resistance of the ATO material. However, its low BET surface area remained conducive for particle agglomeration and support contact area, as evidenced in Figure S2b. This resulted in IrO_x particle detachment lowering the active area further. In contrast, the electrode potential of the IrO_x/ATO catalyst remained relatively constant throughout the 15 h stability test, clearly displaying the most stable behavior. This observation can be rationalized in terms of a high surface area, corrosion-resistant ATO support material.

While the nature of the support materials (carbon or oxides) may plausibly account for the differences in support stability and may hence offer a consistent explanation for the distinct chronopotentiometric trajectories in Figure 7, the support material by itself cannot account for differences in the corrosion behavior of the similarly sized IrO_x particle ensembles of the three catalysts. Here, the oxidation state, surface Ir oxide layer thickness, and surface morphology play key roles that control the corrosion stability. This is why MMOSI effects can offer a physicochemical explanation for stability benefits of oxide-supported versus carbon-supported IrO_x particles.[59] The effective rate of anodic metal dissolution is linked to the rate of metal oxidation, i.e., the oxidizability of the metal.[59] Anodic dissolution increases as Ir atoms take on more positive oxidation states.[59] Conversely, stabilized lower average Ir oxidation states should slow down Ir dissolution. Indeed, Figure S10 displays the measured quantitative Ir loss by dissolution (particle instability) and detachment (support instability) and confirms our conjecture. The trend in Ir dissolution (green portion of bars) follows the trend in oxidation state and the associated relative magnitudes of the MMOSI effect.

In summary, MMOSI effects mitigate rate and extent of Ir oxidation and active particle dissolution at anodic oxidation potentials yet are unable to suppress support degradation and support-degradation-based consequences such as particle detachment.

4.3. Charge-Transfer Rate Analysis of IrO_x Catalysts. Polarization curves and Tafel characteristics of the IrO_x catalysts (Figure 8) recorded before and after the galvanostatic stability test offered potentiostatic insights on the catalytic activity and stability of the IrO_x catalysts. They confirmed the stability trends and conclusions drawn from the galvanostatic chronopotentiometric data. Finally, in the linear Tafel region of the OER reaction potentiostatic electrochemical impedance analyses were carried out to determine changes in the uncompensated ohmic as well as in the differential charge-transfer resistance, R_{ct} (Figure 9), which controls the rate of an interfacial electrode reaction.[77,78] In the linear Tafel region at constant dc overpotentials (here +1.7 V_{RHE}), R_{ct} is related to the electrocatalytic reaction kinetics at constant reactant concentration, c, according to[79−81]

$$R_{ct} = \left(\frac{\partial \eta}{\partial j_{OER}}\right)_c = \frac{RT}{\alpha F j_{OER}} \approx \frac{1}{A_{IrO_x} L_{IrO_x}} \quad (2)$$

Following our arguments above, the sharply increased charge-transfer resistances of the two IrO_x/C and IrO_x/Com. ATO reference catalysts reflect severe losses in the IrO_x surface area, A_{IrO_x}, and the IrO_x particle mass loading, L_{IrO_x}, during the galvanostatic stability test. In contrast, the value of R_{ct} of the IrO_x/ATO catalyst varied only slightly owing to their enhanced stability against electrochemical dissolution via the MMOSI effect (Figure S10).

To show the validity of eq 2 directly in separate controlled experiments, we cross-checked the charge-transfer resistances and Tafel slopes of IrO_x/C and IrO_x/ATO catalysts at 4 different initial IrO_x loadings (10, 3, 1, and 0.3 μg_{IrO_x} cm^{-2}_{geo}). Figures S14 and S15 confirm the near-linear trend between charge-transfer resistance and catalyst loading, L_{IrO_x}, while the Tafel slope remained very similar.

For the IrO_x/C catalyst, however, the charge-transfer resistance (Figure 9) and Tafel slope (Figure 8d) values after the galvanostatic stability test ended up around 10-times larger than those determined at 0.3 μg_{IrO_x} cm^{-2}_{geo} loading (the effective loading after stability test), highlighting the massive loss of *accessible* active IrO_x due to carbon corrosion.

Overall, our present results highlight the role of metal/metal−oxide support interactions (MMOSI) for the corrosion durability of supported IrO_x OER electrocatalysts. In enabling MMOSI effects, antimony-doped tin oxide (ATO) appears to be a suitable support material to reduce the loading of Ir while enhancing the stability of the active Ir particles in acid water electrolyzers. It is possible that similar MMOSI affect the metal corrosion stability in other technologically relevant oxide support/nanoparticle couples like in the Cu/CuO_x system.

5. CONCLUSIONS

We investigated the relation between the electronic structure and the electrochemical stability of supported electrochemically oxidized IrO_x nanoparticles and found spectroscopic evidence for electronic interactions between oxide supports and IrO_x nanoparticles. Such electronic charge interactions were absent or negligible on carbon supports. We termed these interactions metal/metal−oxide support interactions (MMOSI).

In an attempt to deconvolute the role of the support and of the IrO_x nanoparticles in the overall degradation behavior during a galvanostatic stability test, we concluded that the corrosive dissolution stability of the IrO_x particles significantly benefits from the presence of MMOSI effects. The calculated Ir mass loss of IrO_x/ATO after the stability test was 28.3% of their initial Ir loading, while IrO_x/C was 97.1%, which suggests that MMOSI effects help maintain higher IrO_x loading and thus sustained high charge-transfer kinetics.

More specifically, a lower average Ir oxidation state was observed after electrochemical oxidation with IrO_x/ATO ($Ir^{3.2+}$) as compared to IrO_x/C (Ir^{4+}). Therefore, we

DOI: 10.1021/jacs.6b07199
J. Am. Chem. Soc. 2016, 138, 12552−12563

demonstrated that MMOSI effects rendered the voltammetric transformation of metallic Ir to IrO_x more difficult, decreasing the effective IrO_x layer thickness and resulting in a sustained lowering of the Ir oxidation state.

Our findings raise the possibility that MMOSI effects in electrochemistry—largely neglected to date—may be much more important for a deeper understanding of the durability of oxide-supported metal/metal−oxide electrocatalyst than previously thought.

■ ASSOCIATED CONTENT

Supporting Information

The Supporting Information is available free of charge on the ACS Publications website at DOI: 10.1021/jacs.6b07199.

Details on synthesis mechanism of the antimony-doped tin oxide (ATO) and additional data (PDF)

■ AUTHOR INFORMATION

Corresponding Authors

*E-mail: pstrasser@tu-berlin.de.

*E-mail: teschner@fhi-berlin.mpg.de.

Notes

The authors declare no competing financial interest.

■ ACKNOWLEDGMENTS

Financial support by the German Research Foundation (DFG) through grant STR 596/3-1 under the Priority Program 1613 “Regeneratively formed fuels by water splitting” is gratefully acknowledged. The authors kindly thank HZB for allocation of synchrotron radiation beamtime. A.B. received financial support by the German Research Foundation (DFG) through grant STR 596/4-1. The authors acknowledge the help of Dr. Ivo Zizak for the operation of the MySpot beamline.

■ REFERENCES

(1) Carmo, M.; Fritz, D. L.; Mergel, J.; Stolten, D. *Int. J. Hydrogen Energy* **2013**, *38*, 4901.

(2) Barbir, F. *Sol. Energy* **2005**, *78*, 661.

(3) Grigoriev, S. A.; Porembsky, V. I.; Fateev, V. N. *Int. J. Hydrogen Energy* **2006**, *31*, 171.

(4) Siracusano, S.; Van Dijk, N.; Payne-Johnson, E.; Baglio, V.; Aricò, A. S. *Appl. Catal., B* **2015**, *164*, 488.

(5) Reier, T.; Oezaslan, M.; Strasser, P. *ACS Catal.* **2012**, *2*, 1765.

(6) Antolini, E. *ACS Catal.* **2014**, *4*, 1426.

(7) Danilovic, N.; Subbaraman, R.; Chang, K. C.; Chang, S. H.; Kang, Y.; Snyder, J.; Paulikas, A. P.; Strmcnik, D.; Kim, Y. T.; Myers, D.; Stamenkovic, V. R.; Markovic, N. M. *Angew. Chem., Int. Ed.* **2014**, *53*, 14016.

(8) Reier, T.; Pawolek, Z.; Cherevko, S.; Bruns, M.; Jones, T.; Teschner, D.; Selve, S.; Bergmann, A.; Nong, H. N.; Schlögl, R.; Mayrhofer, K. J. J.; Strasser, P. *J. Am. Chem. Soc.* **2015**, *137*, 13031.

(9) Nong, H. N.; Gan, L.; Willinger, E.; Teschner, D.; Strasser, P. *Chemical Science* **2014**, *5*, 2955.

(10) Chen, X.; Chen, G.; Yue, P. L. *J. Phys. Chem. B* **2001**, *105*, 4623.

(11) de Oliveira-Sousa, A.; da Silva, M. A. S.; Machado, S. A. S.; Avaca, L. A.; de Lima-Neto, P. *Electrochim. Acta* **2000**, *45*, 4467.

(12) Ardizzone, S.; Bianchi, C. L.; Cappelletti, G.; Ionita, M.; Minguzzi, A.; Rondinini, S.; Vertova, A. *J. Electroanal. Chem.* **2006**, *589*, 160.

(13) Marshall, A.; Børresen, B.; Hagen, G.; Tsypkin, M.; Tunold, R. *Electrochim. Acta* **2006**, *51*, 3161.

(14) Sharma, S.; Pollet, B. G. *J. Power Sources* **2012**, *208*, 96.

(15) Antolini, E.; Gonzalez, E. R. *Appl. Catal., A* **2009**, *365*, 1.

(16) Mirabile Gattia, D.; Antisari, M. V.; Giorgi, L.; Marazzi, R.; Piscopiello, E.; Montone, A.; Bellitto, S.; Licoccia, S.; Traversa, E. *J. Power Sources* **2009**, *194*, 243.

(17) Dicks, A. L. *J. Power Sources* **2006**, *156*, 128.

(18) Antolini, E. *Appl. Catal., B* **2012**, *123−124*, 52.

(19) Oh, H.-S.; Lim, K. H.; Roh, B.; Hwang, I.; Kim, H. *Electrochim. Acta* **2009**, *54*, 6515.

(20) Oh, H.-S.; Oh, J.-G.; Haam, S.; Arunabha, K.; Roh, B.; Hwang, I.; Kim, H. *Electrochem. Commun.* **2008**, *10*, 1048.

(21) Maass, S.; Finsterwalder, F.; Frank, G.; Hartmann, R.; Merten, C. *J. Power Sources* **2008**, *176*, 444.

(22) Oh, H.-S.; Kim, K.; Kim, H. *Int. J. Hydrogen Energy* **2011**, *36*, 11564.

(23) Huang, H. X.; Chen, S. X.; Yuan, C. *J. Power Sources* **2008**, *175*, 166.

(24) Yu, X.; Ye, S. *J. Power Sources* **2007**, *172*, 133.

(25) Antolini, E.; Gonzalez, E. R. *Solid State Ionics* **2009**, *180*, 746.

(26) Lu, Y.; Jiang, Y.; Gao, X.; Wang, X.; Chen, W. *J. Am. Chem. Soc.* **2014**, *136*, 11687.

(27) Luo, F.; Liao, S.; Dang, D.; Zheng, Y.; Xu, D.; Nan, H.; Shu, T.; Fu, Z. *ACS Catal.* **2015**, *5*, 2242.

(28) Resasco, D. E.; Haller, G. L. *J. Catal.* **1983**, *82*, 279.

(29) Huang, S.-Y.; Ganesan, P.; Park, S.; Popov, B. N. *J. Am. Chem. Soc.* **2009**, *131*, 13898.

(30) Liu, Y.; Mustain, W. E. *J. Am. Chem. Soc.* **2013**, *135*, 530.

(31) Hu, W.; Chen, S.; Xia, Q. *Int. J. Hydrogen Energy* **2014**, *39*, 6967.

(32) Oh, H.-S.; Nong, H. N.; Strasser, P. *Adv. Funct. Mater.* **2015**, *25*, 1074.

(33) Oh, H.-S.; Nong, H. N.; Reier, T.; Gliech, M.; Strasser, P. *Chemical Science* **2015**, *6*, 3321.

(34) Nong, H. N.; Oh, H.-S.; Reier, T.; Willinger, E.; Willinger, M.-G.; Petkov, V.; Teschner, D.; Strasser, P. *Angew. Chem., Int. Ed.* **2015**, *54*, 2975.

(35) Yang, S.; Chung, D. Y.; Tak, Y.-J.; Kim, J.; Han, H.; Yu, J.-S.; Soon, A.; Sung, Y.-E.; Lee, H. *Appl. Catal., B* **2015**, *174−175*, 35.

(36) Park, S.-A.; Lim, H.; Kim, Y.-T. *ACS Catal.* **2015**, *5*, 3995.

(37) Lewera, A.; Timperman, L.; Roguska, A.; Alonso-Vante, N. *J. Phys. Chem. C* **2011**, *115*, 20153.

(38) Jaksic, J. M.; Nan, F.; Papakonstantinou, G. D.; Botton, G. A.; Jaksic, M. M. *J. Phys. Chem. C* **2015**, *119*, 11267.

(39) Campbell, C. T. *Nat. Chem.* **2012**, *4*, 597.

(40) Kumar, A.; Ramani, V. *ACS Catal.* **2014**, *4*, 1516.

(41) Kumar, A.; Ramani, V. *J. Electrochem. Soc.* **2013**, *160*, F1207.

(42) Ho, V. T. T.; Pan, C.-J.; Rick, J.; Su, W.-N.; Hwang, B.-J. *J. Am. Chem. Soc.* **2011**, *133*, 11716.

(43) Nguyen, T.-T.; Ho, V. T. T.; Pan, C.-J.; Liu, J.-Y.; Chou, H.-L.; Rick, J.; Su, W.-N.; Hwang, B.-J. *Appl. Catal., B* **2014**, *154−155*, 183.

(44) Ravel, B.; Newville, M. *J. Synchrotron Radiat.* **2005**, *12*, 537.

(45) Bluhm, H.; Hävecker, M.; Knop-Gericke, A.; Kleimenov, E.; Schlögl, R.; Teschner, D.; Bukhtiyarov, V. I.; Ogletree, D. F.; Salmeron, M. *J. Phys. Chem. B* **2004**, *108*, 14340.

(46) Knop-Gericke, A.; Kleimenov, E.; Hävecker, M.; Blume, R.; Teschner, D.; Zafeiratos, S.; Schlögl, R.; Bukhtiyarov, V. I.; Kaichev, V. V.; Prosvirin, I. P.; Nizovskii, A. I.; Bluhm, H.; Barinov, A.; Dudin, P.; Kiskinova, M. In *Advances in Catalysis*; Bruce, C. G., Helmut, K., Eds.; Academic Press, 2009; Vol. *52*, p 213.

(47) Strasser, P. *J. Comb. Chem.* **2008**, *10*, 216.

(48) Forgie, R.; Bugosh, G.; Neyerlin, K. C.; Liu, Z.; Strasser, P. *Electrochem. Solid-State Lett.* **2010**, *13*, B36.

(49) Oh, H.-S.; Oh, J.-G.; Hong, Y.-G.; Kim, H. *Electrochim. Acta* **2007**, *52*, 7278.

(50) Sinfelt, J. H.; Meitzner, G. D. *Acc. Chem. Res.* **1993**, *26*, 1.

(51) Choy, J.-H.; Kim, D.-K.; Demazeau, G.; Jung, D.-Y. *J. Phys. Chem.* **1994**, *98*, 6258.

(52) Hitchcock, A. P.; Wen, A. T.; Rühl, E. *Chem. Phys.* **1990**, *147*, 51.

(53) Brown, M.; Peierls, R. E.; Stern, E. A. *Phys. Rev. B* **1977**, *15*, 738.

DOI: 10.1021/jacs.6b07199
J. Am. Chem. Soc. 2016, 138, 12552−12563

(54) Clancy, J. P.; Chen, N.; Kim, C. Y.; Chen, W. F.; Plumb, K. W.; Jeon, B. C.; Noh, T. W.; Kim, Y.-J. *Phys. Rev. B: Condens. Matter Mater. Phys.* **2012**, *86*, 195131.
(55) Yoshida, H.; Yuliati, L.; Hamajima, T.; Hattori, T. *Mater. Trans.* **2004**, *45*, 2062.
(56) Choy, J.-H.; Kim, D.-K.; Hwang, S.-H.; Demazeau, G.; Jung, D.-Y. *J. Am. Chem. Soc.* **1995**, *117*, 8557.
(57) Minguzzi, A.; Locatelli, C.; Cappelletti, G.; Scavini, M.; Vertova, A.; Ghigna, P.; Rondinini, S. *J. Phys. Chem. A* **2012**, *116*, 6497.
(58) Reifsnyder, S. N.; Otten, M. M.; Sayers, D. E.; Lamb, H. H. *J. Phys. Chem. B* **1997**, *101*, 4972.
(59) Danilovic, N.; Subbaraman, R.; Chang, K.-C.; Chang, S. H.; Kang, Y. J.; Snyder, J.; Paulikas, A. P.; Strmcnik, D.; Kim, Y.-T.; Myers, D.; Stamenkovic, V. R.; Markovic, N. M. *J. Phys. Chem. Lett.* **2014**, *5*, 2474.
(60) Danilovic, N.; Subbaraman, R.; Chang, K. C.; Chang, S. H.; Kang, Y.; Snyder, J.; Paulikas, A. P.; Strmcnik, D.; Kim, Y. T.; Myers, D.; Stamenkovic, V. R.; Markovic, N. M. *Angew. Chem.* **2014**, *126*, 14240.
(61) Tanuma, S.; Powell, C. J.; Penn, D. R. *Surf. Interface Anal.* **1994**, *21*, 165.
(62) Pfeifer, V.; Jones, T. E.; Velez, J. J. V.; Massue, C.; Greiner, M. T.; Arrigo, R.; Teschner, D.; Girgsdies, F.; Scherzer, M.; Allan, J.; Hashagen, M.; Weinberg, G.; Piccinin, S.; Haevecker, M.; Knop-Gericke, A.; Schloegl, R. *Phys. Chem. Chem. Phys.* **2016**, *18*, 2292.
(63) Reier, T.; Teschner, D.; Lunkenbein, T.; Bergmann, A.; Selve, S.; Kraehnert, R.; Schlögl, R.; Strasser, P. *J. Electrochem. Soc.* **2014**, *161*, F876.
(64) Polonský, J.; Mazúr, P.; Paidar, M.; Christensen, E.; Bouzek, K. *Int. J. Hydrogen Energy* **2014**, *39*, 3072.
(65) Mattos-Costa, F. I.; de Lima-Neto, P.; Machado, S. A. S.; Avaca, L. A. *Electrochim. Acta* **1998**, *44*, 1515.
(66) Gaudet, J.; Tavares, A. C.; Trasatti, S.; Guay, D. *Chem. Mater.* **2005**, *17*, 1570.
(67) Hu, J.-M.; Zhang, J.-Q.; Cao, C.-N. *Int. J. Hydrogen Energy* **2004**, *29*, 791.
(68) De Faria, L. A.; Boodts, J. F. C.; Trasatti, S. *J. Appl. Electrochem.* **1996**, *26*, 1195.
(69) Kim, J.-H.; Chang, S.; Kim, Y.-T. *Appl. Catal., B* **2014**, *158–159*, 112.
(70) Hillman, A. R.; Skopek, M. A.; Gurman, S. J. *Phys. Chem. Chem. Phys.* **2011**, *13*, 5252.
(71) Tew, M. W.; Miller, J. T.; van Bokhoven, J. A. *J. Phys. Chem. C* **2009**, *113*, 15140.
(72) Akalework, N. G.; Pan, C.-J.; Su, W.-N.; Rick, J.; Tsai, M.-C.; Lee, J.-F.; Lin, J.-M.; Tsai, L.-D.; Hwang, B.-J. *J. Mater. Chem.* **2012**, *22*, 20977.
(73) Pauporté, T.; Aberdam, D.; Hazemann, J.-L.; Faure, R.; Durand, R. *J. Electroanal. Chem.* **1999**, *465*, 88.
(74) Neyerlin, K. C.; Gu, W.; Jorne, J.; Gasteiger, H. A. *J. Electrochem. Soc.* **2007**, *154*, B631.
(75) Meier, J. C.; Galeano, C.; Katsounaros, I.; Topalov, A. A.; Kostka, A.; Schüth, F.; Mayrhofer, K. J. J. *ACS Catal.* **2012**, *2*, 832.
(76) Shao, Y.; Yin, G.; Gao, Y. *J. Power Sources* **2007**, *171*, 558.
(77) Gileadi, E. *Electrode Kinetics for Chemists, Chemical Engineers, and Material Scientists*; VCH Publishing: New York, 1993.
(78) Hamann, C. H.; Hamnett, A.; Vielstich, W. *Electrochemistry*; Wiley, 2007.
(79) Sen Gupta, S.; Mahapatra, S. S.; Datta, J. *J. Power Sources* **2004**, *131*, 169.
(80) Zhao, J.; Manthiram, A. *J. Electrochem. Soc.* **2011**, *158*, B208.
(81) Malevich, D.; Halliop, E.; Peppley, B. A.; Pharoah, J. G.; Karan, K. *J. Electrochem. Soc.* **2009**, *156*, B216.

DOI: 10.1021/jacs.6b07199
J. Am. Chem. Soc. 2016, 138, 12552–12563